

MICROWAVE SKY SIMULATIONS AND PROJECTIONS FOR GALAXY CLUSTER DETECTION WITH THE ATACAMA COSMOLOGY TELESCOPE

NEELIMA SEHGAL

Department of Physics and Astronomy, Rutgers University, Piscataway, NJ 08854

HY TRAC

Department of Astrophysical Sciences, Princeton University, Princeton, NJ 08544

KEVIN HUFFENBERGER

Jet Propulsion Laboratory, Pasadena, CA 91109; and California Institute of Technology, Pasadena, CA 91125

AND

PAUL BODE

Department of Astrophysical Sciences, Princeton University, Princeton, NJ 08544

Received 2006 December 6; accepted 2007 April 16

ABSTRACT

We study the ability of three-frequency, arcminute-resolution microwave measurements to detect galaxy clusters via their Sunyaev-Zel'dovich (SZ) distortion of the microwave background. For this purpose, we have constructed large-area simulations of the microwave sky, and we have made them publicly available to further investigations into optimal data reduction techniques for upcoming SZ cluster surveys. In these sky simulations, galaxy clusters are modeled using N -body simulated dark matter halos plus a gas prescription for the intracluster medium that allows the small-scale cluster physics such as star formation and feedback to be realistically incorporated. We also model the primary microwave background, radio and infrared point sources, galactic dust emission, and the SZ flux including kinetic and relativistic contributions. We make use of these simulations to study the scaling relation between integrated SZ flux and cluster mass and find that our clusters follow a power law with an index that is steeper than that for self-similar cluster models. Some evolution of the power-law index and normalization with redshift is also observed. These simulations are also used to study cluster detection for the Atacama Cosmology Telescope (ACT). Using a multifrequency Wiener filter to separate clusters from other microwave components, we find that ACT alone can recover a cluster sample that is $\approx 90\%$ complete and $\approx 85\%$ pure above $3 \times 10^{14} M_{\odot}$.

Subject headings: cosmology: theory — galaxies: clusters: general — intergalactic medium

1. INTRODUCTION

Cluster catalogs provide valuable information on the evolution and distribution of matter over cosmic time. It has long been realized that the abundance of galaxy clusters as a function of redshift is a sensitive probe of the underlying cosmology (e.g., Oukbir & Blanchard 1992; Eke et al. 1996; Viana & Liddle 1996; Barbosa et al. 1996; Bahcall & Fan 1998; Rosati et al. 2002). It has also been appreciated that a large sample of galaxy clusters can provide important constraints on the dark energy density and equation of state that are complementary to those obtained from microwave background and Type Ia supernovae measurements (e.g., Wang & Steinhardt 1998; Haiman et al. 2001; Weller et al. 2002; Weller & Battye 2003; Majumdar & Mohr 2003; Wang et al. 2004; Lima & Hu 2005). This has prompted efforts to obtain cluster catalogs from wide, deep surveys.

Searches for clusters based on their Sunyaev-Zel'dovich (SZ) effect (Sunyaev & Zel'dovich 1970, 1972) have a particular advantage over X-ray and optical searches since the SZ signal does not dim at high redshifts ($z > 1$), where the cluster abundance is strongly dependent on cosmology (for reviews on the SZ effect see Birkinshaw 1999; Carlstrom et al. 2002). In light of this, there are a host of ground-based bolometer array instruments (ACBAR, ACT, APEX, SPT) and interferometers (AMI, AMiBA, SZA) either online or scheduled to come online in the next few years that potentially will detect hundreds to thousands of clusters at microwave frequencies via their SZ effect (Runyan et al. 2003;

Kosowsky 2003; Güsten et al. 2006; Ruhl et al. 2004; Kneissl et al. 2001; Li et al. 2006). The *Planck* satellite, to be launched in 2008, should also provide an all-sky map of massive clusters in the microwave band (Tauber 2004).

Using cluster catalogs to constrain cosmology requires a solid understanding of the cluster selection criteria. A given survey's cluster selection function is intimately tied to characteristics of the instrument and data reduction techniques. Considerable attention has been devoted to exploring various data reduction methods for different SZ surveys. This has been pursued in an effort to study both the optimal detection of clusters and the optimal recovery of the cluster SZ flux. The former consists of maximizing the completeness and minimizing the contamination of a given cluster sample. The latter is necessary to properly identify the observable (SZ flux) with mass, or to employ self-calibration schemes to fit for the SZ flux-mass relation and cosmology simultaneously (Majumdar & Mohr 2004; Younger et al. 2006).

Various filtering approaches have been utilized to isolate the SZ signal and extract clusters in simulations. Such techniques have employed matched filters (Herranz et al. 2002a, 2002b), Wiener filters (Aghanim et al. 1997), wavelet filters (Pierpaoli et al. 2005), and maximum entropy methods (Stolyarov et al. 2002). Several papers have implemented versions of these filters and begun careful study of selection functions for upcoming SZ surveys (Schulz & White 2003; White 2003; Melin et al. 2005, 2006; Vale & White 2006; Schaefer & Bartelmann 2006; Juin et al. 2007). With this in mind, we have created a large-scale simulation

of the microwave sky on which these data reduction techniques can be refined.

To model the SZ flux accurately generally requires expensive, high-resolution hydrodynamic simulations to realistically model the small-scale cluster physics. However, it is a challenge to create such simulations in a large enough volume so that one is not limited by cosmic variance when performing statistical studies. To overcome this challenge, we create a cluster catalog using an N -body simulation combined with a gas prescription given by Ostriker et al. (2005). The N -body code only needs to be run once for a given cosmology, and the small-scale cluster physics (including nonspherically symmetric gas distributions, star formation, and feedback) are added afterward via the gas prescription. As a result, the cluster physics can be varied easily without having to redo expensive runs.

These cluster simulations were incorporated within microwave sky simulations consisting of two strips of the sky, each 4° wide in declination and 360° around in right ascension. One strip is centered at a declination of -5° , and the other is centered at a declination of -55° , to match the portion of sky that the Atacama Cosmology Telescope (ACT) will observe. The galaxy clusters within this simulation have halo masses down to $5 \times 10^{13} M_\odot$, and the N -body simulation employs the latest cosmological parameters derived from a combination of WMAP3, SDSS, *Hubble Space Telescope* (HST), and SN Astier observations ($\Omega_m = 0.26$, $\Omega_\Lambda = 0.74$, $\Omega_b = 0.044$, $n = 0.95$, $\sigma_8 = 0.77$, $h = 0.72$; see Spergel et al. 2007 and references therein). We include the full SZ effect, with relativistic corrections, as well as infrared and radio point sources (uncorrelated with clusters), using number counts given by Borys et al. (2003; infrared) and Knox et al. (2004; radio). Galactic dust and primary microwave background fluctuations are also modeled, the latter generated using the *WMAP* ILC map (Bennett et al. 2003a; Hinshaw et al. 2007). These sky simulations were made at the observing frequencies of 145, 215, and 280 GHz and are in a cylindrical equal-area sky projection (Calabretta & Greisen 2002). The final sky maps are in a standard FITS format and have a pixel size of $\approx 0.2' \times 0.2'$ and units of Jy sr^{-1} . A catalog of all the cluster halos in the simulation is also provided, specifying each halo's basic properties. These microwave sky simulations are available online.¹

We use these simulations to study the scaling relation between SZ flux and cluster mass, as well as prospects for cluster detection with ACT. Roughly 10^5 clusters are used to determine the simulated SZ flux-mass scaling relation. We compare cluster M_{200} to Y_{200} , which we take to be the SZ Compton y -parameter integrated over a disk of radius R_{200} . These clusters are fitted to a power-law relation between $Y_{200}E(z)^{-2/3}$ and M_{200} , and estimates of the power-law index and normalization are given.

We also employ a multifrequency Wiener filter and simple peak-finding algorithm to forecast cluster detection given ACT instrument specifications. Since there has been considerable interest of late in how point-source contamination affects cluster detection (e.g., Melin et al. 2006), this is investigated under three different contamination assumptions: no point sources, only infrared point sources, and both infrared and radio point sources. Completeness of our recovered cluster sample is given as a function of both M_{200} and Y_{200} (in units of arcmin^2), the latter being directly obtainable from microwave observations. We also give the purity of our projected cluster sample, where purity is one minus the percentage of false-positive detections. The issue of optimal SZ flux recovery for individual clusters is left to later work.

The outline of this paper is as follows. In § 2 we give the simulation details. Section 3 consists of an investigation of the Y - M relation as suggested by our simulations, and § 4 gives cluster detection projections for ACT. In § 5 we discuss directions for future work, and in § 6 we summarize and conclude.

2. SIMULATIONS

2.1. Simulated Clusters

2.1.1. The Dark Matter Run

Initial conditions for the N -body run were generated with the GRAFIC2 code (Bertschinger 2001), available online.² As written, this code uses a spherical Hanning filter on small scales. However, we have found that this filter significantly suppresses power on these scales, so we removed it from use. GRAFIC2 perturbs particles from a regular grid using the Zel'dovich approximation. The simulation started at redshift $z = 35.3$, when the initial density fluctuation amplitude on the scale of this grid was 10%. $N = 1024^3 \approx 10^9$ particles were contained in a periodic box of size $L = 1000 h^{-1} \text{ Mpc}$, so the particle mass is thus $6.72 \times 10^{10} h^{-1} M_\odot$. The cubic spline softening length was set to $\epsilon = 16.276 h^{-1} \text{ kpc}$. The simulation was carried out with the tree-particle-mesh (TPM) code (Bode et al. 2000; Bode & Ostriker 2003), modified slightly from the publicly available version.³ Particle positions and velocities were followed at double precision, although acceleration was kept at single precision. Also, no lower limit was set to the parameter B used in domain decomposition (see eq. [5] of Bode & Ostriker 2003), which at late times results in more particles being followed at full force resolution. The initial domain decomposition parameters used are $A = 1.9$ and $B = 9.2$. The particle-mesh (PM) contained 2048^3 cells, and the maximum subbox was 256 cells. By the end of the run, 5×10^6 trees containing 54% of the particles were followed at full resolution. More details of the simulation are in Bode et al. (2007).

At each PM time step, the matter distribution in a thin shell is saved. The radius of the shell corresponds to the light-travel time from a $z = 0$ observer sitting at the origin of the box, and its width corresponds to the time step interval. The portion of a spherical shell covering one octant of the sky was saved, so for comoving distances larger than $1000 h^{-1} \text{ Mpc}$ there can be some duplication in structures as the periodic box is repeated. However, while there are repeated dark matter halos in the simulations, the repetition is usually at a different redshift, so the dynamical state is different. In cases where a cluster appears twice at the same redshift, it is viewed at two different angles, making each projected image unique. At the end of the simulation, the full matter distribution in a light cone extending to $z = 3$ was saved in 417 time slices. Dark matter halos in this light cone were identified with the friends-of-friends (FoF) algorithm using a linking parameter $b = 0.2$ (i.e., the linking length is one-fifth of the mean interparticle separation of the simulation, or $195 h^{-1} \text{ kpc}$ comoving). A $5 \times 10^{13} h^{-1} M_\odot$ cluster contains 744 particles.

As shown in Figure 1, the halo mass functions measured from the simulated light cone agree well with the semianalytic fitting formula from Jenkins et al. (2001) for an FoF linking length $b = 0.2$. The number of halos above a minimum mass per unit redshift per 100 deg^2 is plotted for three minimum masses $M_{\min} = (1, 2, 4) \times 10^{14} h^{-1} M_\odot$. The data points are measured using all halos in the octant to minimize sample variance, but then they are normalized to 100 deg^2 . For any cluster survey, the minimum detectable mass is likely to be a function of redshift, and the three

¹ See <http://www.astro.princeton.edu/~act/>.

² See <http://web.mit.edu/edbert/>.

³ See <http://www.astro.princeton.edu/~bode/TPM/>.

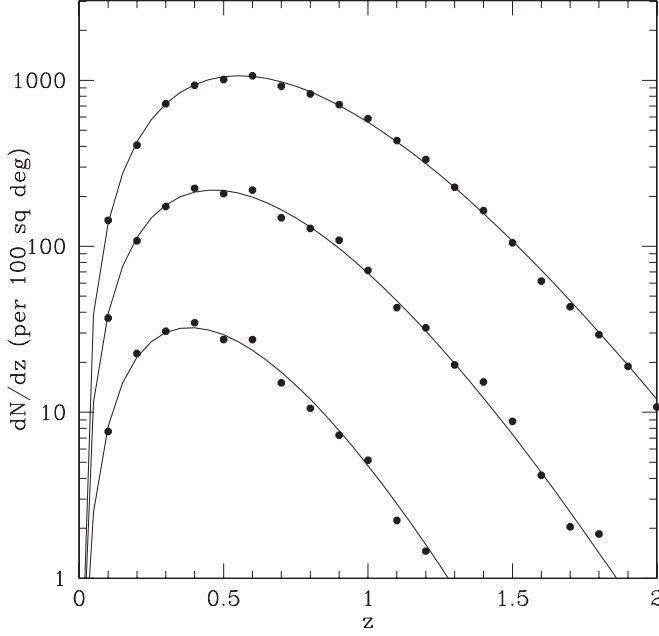


FIG. 1.—Halo abundance above a minimum mass per unit redshift per 100 deg² measured from the simulation compared with the semianalytic fitting formula from Jenkins et al. (2001). From top to bottom, the three sets of points are for the minimum masses $M_{\min} = (1, 2, 4) \times 10^{14} h^{-1} M_{\odot}$.

values chosen reflect the range expected for the upcoming SZ surveys.

2.1.2. Adding Gas to Dark Matter Halos

Gas is added to each cluster following the prescription of Ostriker et al. (2005) and Bode et al. (2007). For each dark matter halo, the gravitational potential is found on a mesh with cell size $2\epsilon = 32.552 h^{-1}$ kpc. The gas density and pressure (or temperature) are found in each cell by assuming that it is in hydrostatic equilibrium and has a polytropic equation of state with adiabatic index $\Gamma = 1.2$. It is also assumed that initially the baryon fraction inside the virial radius is Ω_b/Ω_m , and that the energy per unit mass of the baryons equals that of the dark matter. To specify the central density and pressure with these assumptions requires two constraints.

The first constraint is the pressure at the virial radius, which is the radius enclosing the virial overdensity calculated from spherical top-hat collapse (this is a slight change from Ostriker et al. [2005], which used an overdensity of 200 times critical). The dark matter kinetic energy is found in a buffer region extending for nine cells outside of the virial radius. This is then translated into a surface pressure, P_s , by assuming that the velocity dispersion is isotropic and the baryon fraction in this region equals the cosmic mean. The second constraint is conservation of energy. The final energy of the gas must equal this initial energy, after adjusting for any of the effects that can cause changes in energy.

One such effect is that the gas distribution inside the cluster can expand or contract. This can, for example, reduce the baryon fraction inside the virial radius if the gas distribution expands further out. This would also reduce the energy of the gas as it does mechanical work pushing against the surface pressure. The surface pressure is assumed to remain at P_s wherever the final gas radius ends up.

Star formation will also affect gas energy. At $z = 0$, it is assumed that the stellar-to-gas mass ratio is 0.10. The star formation

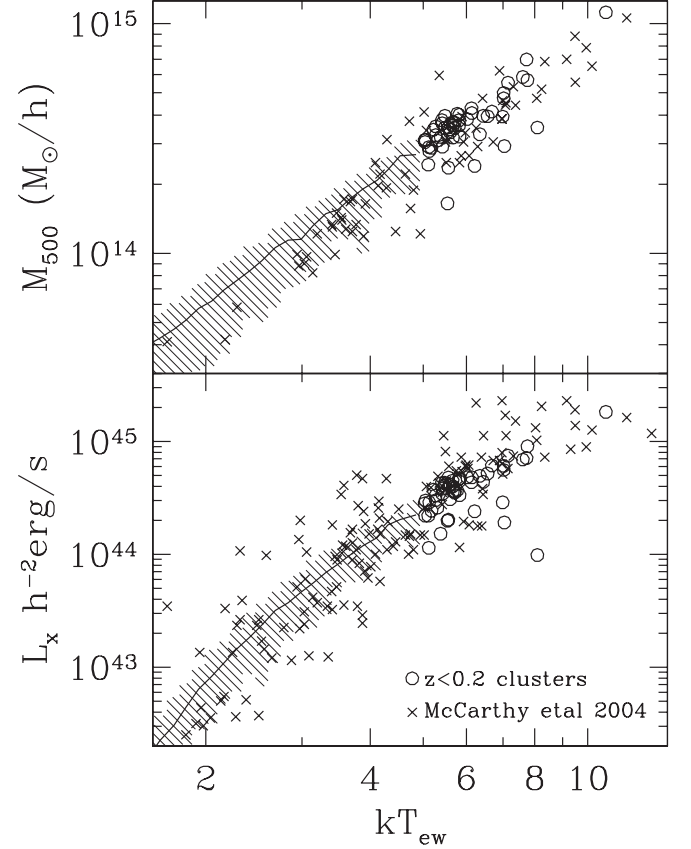


FIG. 2.— M_{500} - T and L_X - T relations for the simulated clusters below $z = 0.2$ compared to those from observed X-ray clusters. The open circles are the simulated clusters above $kT_{\text{ew}} = 5$ keV. The median value of the simulated clusters below 5 keV is represented by a solid line, with the shaded region enclosing 90% of the clusters. T_{ew} is the emission-weighted X-ray temperature.

rate is assumed to follow a delayed exponential model (eq. [1] of Nagamine et al. 2006) with decay time $\tau = 1$ Gyr, so at higher redshift the star/gas mass ratio can be calculated. To make stars, the gas with the largest initial binding energy is removed, thus changing the total energy budget. Furthermore, some fraction of the rest mass turned into stars is taken to be converted into thermal energy in the gas, via supernovae and active galactic nuclei. The energy added to the intracluster medium by these processes can be written as $\epsilon_f M_* c^2$, where M_* is the stellar mass and the feedback efficiency is estimated to be $\epsilon_f = 5 \times 10^{-5}$. This value is determined by fitting to X-ray observations of nearby clusters (Bode et al. 2007); at $z = 0$, this added energy amounts to roughly 3 keV per particle.

The top panel of Figure 2 shows the resulting M_{500} - T relation for all the clusters in the light cone at low redshift, $z < 0.2$. The temperature used is the X-ray emission-weighted temperature inside R_{500} . The $kT > 5$ keV clusters are shown as open circles, and, for clarity, the median value of the clusters below 5 keV is shown as a line, with the shaded region enclosing 90% of the clusters. Shown for comparison are data derived from X-ray clusters over the same redshift range, taken from Reiprich & Böhringer (2002) as adjusted by McCarthy et al. (2004). The simulated sample reproduces the observed M_{500} - T relation quite well. The gas temperature (or pressure) is fairly insensitive to the exact choice of ϵ_f . Feedback has much more of an effect on gas density, making the L_X - T relation a more exacting comparison (Bode et al. 2007). This relation is shown in the bottom panel of Figure 2, along with data points taken from the *ASCA* cluster catalog (Horner 2001) as



FIG. 3.—Sample image showing the fully relativistic SZ signal at 145 GHz. The image dimensions are 33° across in right ascension by 4° wide in declination centered at $\delta = -55^\circ$. Black represents $\Delta T/T_{\text{CMB}}$ greater than -6×10^{-6} , and white represents $\Delta T/T_{\text{CMB}}$ less than -10×10^{-6} . The former value is chosen to be representative of ACT instrument noise in $0.2'$ pixels.

described in McCarthy et al. (2004). Again, the simulated clusters agree with the observed relation.

2.2. Simulated SZ Signal

For each of the simulated clusters, the gas prescription gives us the electron number density n_e , temperature T_e , and velocity v fields with which to model the SZ effect, including relativistic corrections. We assume that the gas is fully ionized with a helium mass fraction equal to 0.24. The change in the microwave background intensity after passing through a path length dl in the direction \hat{n} is given by

$$\begin{aligned} \frac{\Delta I_\nu}{I_0} = & \frac{X^4 e^X}{(e^X - 1)^2} d\tau \theta_e (Y_0 + \theta_e Y_1 + \theta_e^2 Y_2 + \theta_e^3 Y_3 + \theta_e^4 Y_4) \\ & + \frac{X^4 e^X}{(e^X - 1)^2} d\tau \left(\frac{v}{c}\right)^2 \left[\frac{1}{3} Y_0 + \theta_e \left(\frac{5}{6} Y_0 + \frac{2}{3} Y_1\right)\right] \\ & + \frac{X^4 e^X}{(e^X - 1)^2} d\tau \frac{v_{\text{los}}}{c} (1 + \theta_e C_1 + \theta_e^2 C_2), \end{aligned} \quad (1)$$

where

$$I_0 \equiv 2(k_B T_{\text{CMB}})^3 / (hc)^2, \quad (2)$$

$$X \equiv h\nu / k_B T_{\text{CMB}}, \quad (3)$$

$$\theta_e \equiv k_B T_e / m_e c^2, \quad (4)$$

and Y and C are known frequency-dependent coefficients (Nozawa et al. 1998). The usual Compton y -parameter is given by

$$y \equiv \int \theta_e d\tau = \frac{k_B \sigma_T}{m_e c^2} \int n_e T_e dl, \quad (5)$$

where $d\tau = \sigma_T n_e dl$ is the optical depth through a path length dl . The first-order (nonrelativistic) thermal and kinetic SZ signals are given by

$$\left(\frac{\Delta T}{T_{\text{CMB}}}\right)_{\text{tsz}} \equiv y Y_0 = y [X \coth(X/2) - 4] \quad (6)$$

and

$$\left(\frac{\Delta T}{T_{\text{CMB}}}\right)_{\text{ksz}} \equiv \int \left(\frac{v_{\text{los}}}{c}\right) d\tau = \sigma_T \int n_e \left(\frac{v_{\text{los}}}{c}\right) dl, \quad (7)$$

respectively, where v_{los} is the line-of-sight component of the peculiar velocity field. For a 10 keV cluster with $v_{\text{los}} = 1000 \text{ km s}^{-1}$, the correction to the first-order thermal SZ from the $O(d\tau \theta_e^2)$ term at 145 GHz is about 7.5%, but it becomes considerably more substantial near the null of the thermal SZ. The terms $O(d\tau v_{\text{los}} \theta_e)$ and $O(d\tau v_{\text{los}} \theta_e^2)$ give about 8% and 1% corrections to the first-order kinetic SZ (Nozawa et al. 1998). Note that the factor

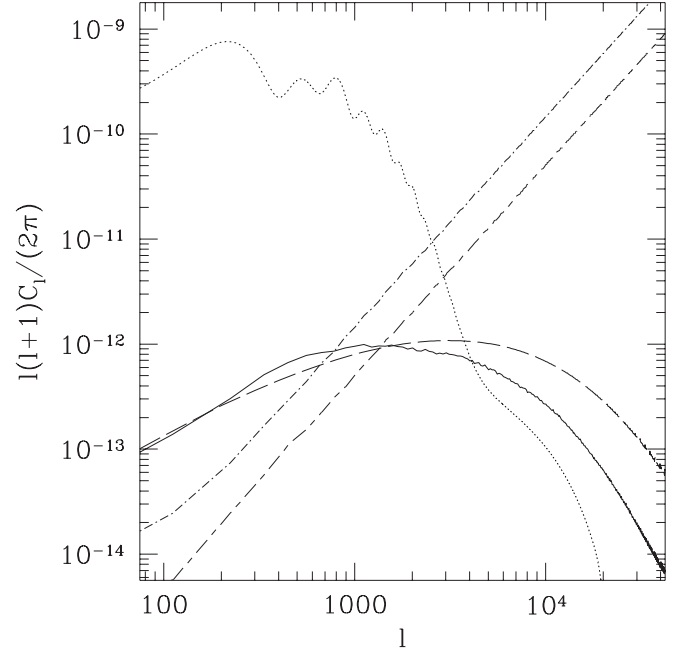


FIG. 4.—Solid line: First-order thermal SZ power spectrum at 145 GHz from the simulation. Dashed line: First-order thermal SZ power spectrum at 145 GHz derived analytically from Komatsu & Seljak (2002). For comparison, we include the lensed primary microwave background power spectrum derived from CAMB (Challinor & Lewis 2005) for our input cosmology (dotted line) and the power spectrum of infrared (dot-dashed line) and radio (short-dashed–long-dashed line) point sources from the simulation, also at 145 GHz. The radio source power spectrum includes only sources fainter than 35 mJy. Note that C_l is in dimensionless units of $(\Delta T/T)^2$.

$X^4 e^X / (e^X - 1)^2$ in equation (1) converts between $\Delta T/T_{\text{CMB}}$ and $\Delta I_\nu / I_0$.

Sky maps at the ACT observing frequencies of 145, 215, and 280 GHz are made by tracing through the clusters and projecting them onto a cylindrical equal-area grid. Two strips of the sky, each 4° wide in declination and 360° around in right ascension, are constructed and centered at $\delta = -5^\circ$ and -55° , respectively. Since the simulation light cone covers an octant, only one-quarter of the strip is unique and the other three-quarters are mirrored. The accompanying cluster catalog contains the following information: redshift, right ascension, declination, M_{FoF} , M_{200} , M_{500} , R_{200} , R_{500} , and integrated SZ and X-ray properties. (M_{FoF} is the FoF derived mass and M_{200} and M_{500} are the cluster masses within R_{200} and R_{500} , respectively, where the latter are the radii at which the cluster mean density is 200 and 500 times the critical density at the cluster redshift.) Figure 3 is a sample image showing the fully relativistic SZ signal at 145 GHz. This image is 33° across in right ascension and 4° wide in declination, centered at $\delta = -55^\circ$. Black represents $\Delta T/T_{\text{CMB}}$ greater than -6×10^{-6} , and white represents $\Delta T/T_{\text{CMB}}$ less than -10×10^{-6} . The former value is chosen to be representative of ACT instrument noise in $0.2'$ pixels.

In Figure 4, the first-order thermal SZ power spectrum from the simulated map at 145 GHz is compared with a semianalytic prediction derived following the prescription of Komatsu & Seljak (2002). On large angular scales, $l \sim 100$, the two spectra are in agreement, but deviations on smaller scales are found. This is to be expected, since our gas prescription accounts for star formation and feedback that reduce the gas density within clusters (Ostriker et al. 2005; Bode et al. 2007), resulting in a suppression of power on small ($l \gtrsim 1000$) scales. In addition, the feedback pushes the gas out to larger radii and increases the overall temperature of the cluster, leading to an enhancement of power on scales

$l \lesssim 1000$. This demonstrates that one must have a good understanding of baryonic physics within clusters in order to extract cosmology from the SZ power spectrum. Conversely, if the cosmology is well determined, then one can learn about cluster physics from the detected SZ signal.

2.3. Simulated Primary CMB, Point Sources, and Galactic Dust

A primary microwave background map is constructed to have the same large-scale structure as we observe on the sky and small-scale structure consistent with theoretical expectations. For our large-scale map, we use the *WMAP* ILC map (Bennett et al. 2003a; Hinshaw et al. 2007). For $l < 20$, the a_{lm} values are taken from the ILC map with no modification. At smaller scales, the ILC map is smoothed, so a Gaussian random field is added such that the ensemble average power equals the theoretical power spectrum taken from the *WMAP* LAMBDA Web site.⁴ We generate a map with HEALPix parameter $N_{\text{side}} = 4096$ (totaling 201,326,592 pixels). This is then interpolated onto the cylindrical coordinate system using the bilinear interpolation subroutine included in the HEALPix distribution (Górski et al. 2005).

The point sources are drawn from prescribed number counts. For a given flux bin of width ΔS , the number of sources in the survey is drawn from a Poisson distribution with mean $|dN(>S)/dS|\Delta S\Delta\Omega$. Within the bin, each source is assigned a random flux. We choose logarithmic bins that are narrow compared to the range of source fluxes. Each set of sources has flux counts tallied at some reference frequency ν_0 . We scale the source flux from this frequency using a power law, $S \propto (\nu/\nu_0)^\alpha$. Here α is a random variable, chosen for each source from a Gaussian distribution with mean $\bar{\alpha}$ and variance σ_α^2 unique to each source population. For radio sources we use Knox et al. (2004) number counts and choose $\bar{\alpha} = -0.3$ and $\sigma_\alpha = 0.3$ for scaling parameters. *WMAP* found a flatter spectrum with similar variance, but counts are expected to steepen above 100 GHz. For infrared sources we use Borys et al. (2003) number counts and choose $\bar{\alpha} = 3$ and $\sigma_\alpha = 0.5$.

For the contribution of galactic thermal dust emission, we use the “model 8” prediction from Finkbeiner et al. (1999), an extrapolation to microwave frequencies of the dust maps of Schlegel et al. (1998). This model is a two-component fit to *IRAS*, *DIRBE*, and *FIRAS* data and is shown by Bennett et al. (2003b) to be a reasonable template for dust emission in the *WMAP* maps. We create these galactic dust emission maps for completeness of the simulations. However, we do not currently include these dust maps when we investigate cluster detection.

3. Y - M SCALING RELATION

We would like to better understand the relation between SZ flux and mass because this relation reflects cluster physics and also provides the link between SZ cluster catalogs and cosmological parameters, which are constrained by the cluster distribution as a function of mass. A more informed understanding about how changes in cluster physics and cosmology alter the Y - M relation will allow for more information about cosmological parameters to be derived from cluster surveys.

To investigate the SZ flux–mass cluster scaling relation, the integrated Compton y -parameter is compared to cluster mass for the clusters in our simulation. The integrated Compton y -parameter is the Compton y -parameter integrated over the face of the cluster,

i.e., $Y = (\int y d\Omega) d_A^2(z)$, where $d_A^2(z)$ is the angular diameter distance. In the self-similar model, a virialized halo of mass M_{vir} has a virial temperature equal to

$$T_{\text{vir}} \propto [M_{\text{vir}} E(z)]^{2/3}, \quad (8)$$

where for a flat Λ CDM cosmology

$$E(z) = [\Omega_m(1+z)^3 + \Omega_\Lambda]^{1/2}. \quad (9)$$

If clusters were isothermal, we would expect them to satisfy the relation

$$Y \propto f_{\text{gas}} M_{\text{halo}} T, \quad (10)$$

where f_{gas} is the cluster gas mass fraction. Thus, we find

$$Y \propto f_{\text{gas}} M_{\text{vir}}^{5/3} E(z)^{2/3} \quad (11)$$

for the self-similar SZ flux-mass scaling relation. Since clusters are not isothermal and not always in virial equilibrium, deviations from the self-similar relation are expected. Moreover, variation of f_{gas} with redshift and cluster processes such as star formation and feedback can also cause deviations from self-similarity.

From the cluster catalog described in § 2, we choose a subsample with $M_{200} > 7.5 \times 10^{13} M_\odot$ to stay well above our catalog mass limit of $5 \times 10^{13} M_\odot$ and ensure catalog completeness. This leaves us with a sample of about 10^5 clusters. For each cluster, we calculate Y_{200} , which is the projected SZ Compton y -parameter in a disk of radius R_{200} . Clusters are then ranked by mass, and for bins of 250 clusters each, the mean of M_{200} and the mean and standard deviation on the mean of $Y_{200} E(z)^{-2/3}$ are calculated in each bin. These values are plotted in Figure 5. We then fit these values to the power-law relation

$$\frac{Y_{200}}{E(z)^{2/3}} = 10^\beta \left(\frac{M_{200}}{10^{14} M_\odot} \right)^\alpha. \quad (12)$$

We find $\alpha = 1.876 \pm 0.005$ and $\beta = -5.4774 \pm 0.0009$ with a reduced χ^2 of 1.004. This suggests that the Y - M relation is close to a power law. This slope is steeper than that for the self-similar model given in equation (11). This steepening is expected since we assume that feedback is independent of total cluster mass. Energy input of roughly 3 keV per particle will clearly have a relatively larger effect on small clusters with lower virial velocities than on more massive ones. The feedback reduces the gas mass fraction more in lower mass clusters, as more gas is pushed out in proportion to the cluster’s total mass (i.e., the gas fraction inside R_{200} is smaller). As a result, Y_{200} is also decreased more in the lower mass clusters. The power-law index that we find is slightly steeper than that found by some hydrodynamic simulations (e.g., Nagai 2006; Motl et al. 2005; White et al. 2002). This is understandable since we include feedback from active galactic nuclei as well as supernovae, which is different from the hydrodynamic simulations, and the increased level of feedback steepens the slope. It has been estimated that the feedback from active galactic nuclei may be roughly an order of magnitude larger than that from supernovae (Ostriker et al. 2005), so it potentially has a significant effect. The slope we find is also in between that found by da Silva et al. (2004) for their hydrodynamic simulations including radiative cooling alone and cooling plus preheating.

⁴ See http://lambda.gsfc.nasa.gov/product/map/dr2/params/lcdm_all.cfm.

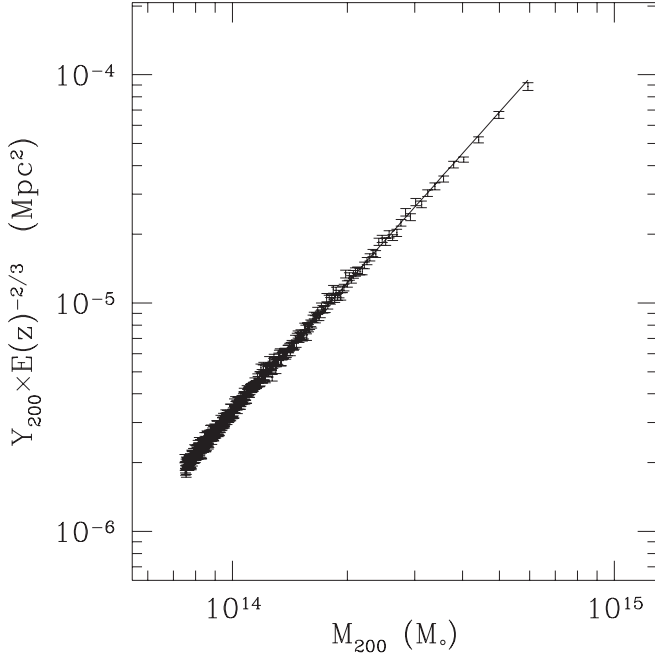


FIG. 5.— $Y_{200}E(z)^{-2/3}$ vs. M_{200} for $\approx 10^5$ clusters within the N -body plus gas simulation. Each point represents the mean value for 250 clusters, and error bars represent the error on the mean. The parameters and reduced χ^2 for the best-fit line are given in Table 2.

A departure from a power law is observed when we restrict our cluster sample to have higher minimum masses. As the minimum mass of the sample is increased, the power-law index gets flatter, illustrating the important effect of feedback on low-mass clusters, as well as the fact that the lowest mass clusters dominate the slope of the Y - M relation because their numbers increase rapidly as mass is decreased. We illustrate this departure in Table 1, where we have performed a similar analysis as above for clusters with $M_{200} > 2 \times 10^{14} M_{\odot}$, this time using bins of 20 clusters each. We find $\alpha = 1.81 \pm 0.02$ and $\beta = -5.463 \pm 0.009$ with a reduced χ^2 of 1.14. This departure indicates that while the Y - M relation is close to a power law, there is some curvature.

We also divide our clusters above $M_{200} > 0.75 \times 10^{14} M_{\odot}$ into four different redshift bins [$z < 0.3$, $z \in (0.3, 0.6)$, $z \in (0.6, 0.9)$, and $z \in (0.9, 1.5)$] to see the evolution of the power-law index and normalization with redshift. The best-fit lines to $Y_{200}E(z)^{-2/3}$ versus M_{200} are shown in Figure 6, and the best-fitted α and β are given in Table 2. Some slight evolution of the power-law index and normalization with redshift is apparent. This is expected since clusters are not perfectly self-similar. Furthermore, the stellar-to-gas mass ratio is a function of redshift in our simulations, and thus the feedback, which is proportional to the star formation, is also a function of redshift. Since more feedback lowers Y disproportionately at the low-mass end, we find the steepest slope for the clusters with $z < 0.3$, which have undergone more star formation and feedback. We find the flattest slope for the clusters in the highest redshift bin. Examining only the higher mass clusters, $M_{200} > 2 \times 10^{14} M_{\odot}$, we see little obvious evolution with redshift of the slope and normalization considering their respective error bars (see Table 1). This again suggests that the higher mass clusters are less sensitive to feedback processes.

The scatter that we find for this Y - M relation is most likely underestimated, as we assume that the gas is described by hydrostatic equilibrium, a single constant polytropic index, and the same amount of feedback per stellar mass for all clusters. Also, we have not included other sources of nonthermal pressure support

TABLE 1
BEST-FIT PARAMETERS FOR CLUSTERS WITH $M_{200} > 2 \times 10^{14} M_{\odot}$,
FITTED USING THE POWER LAW GIVEN IN EQUATION (12)

$M_{200} > 2 \times 10^{14} M_{\odot}$	α	σ_{α}	β	σ_{β}	Reduced χ^2	Clusters	Bins
$z > 0$	1.81	0.02	-5.463	0.009	1.14	7960	398
$z < 0.3$	1.85	0.05	-5.48	0.02	1.05	940	47
$z = 0.3-0.6$	1.78	0.03	-5.44	0.01	1.11	3080	154
$z = 0.6-0.9$	1.85	0.04	-5.49	0.02	1.48	2420	121
$z = 0.9-1.5$	1.82	0.05	-5.46	0.02	0.78	1400	70

that may contribute nonnegligibly to the total pressure. Some of these effects, such as turbulent pressure (see Rasia et al. 2004), are included in all current high-resolution hydrodynamic simulations of galaxy clusters. Initial attempts have also been made to include such effects as magnetic fields (e.g., Dolag et al. 1999) and cosmic rays (Pfrommer et al. 2007). Hydrodynamic simulations can provide a robust check and calibration for semianalytic models, but continuing work is required to include all of the relevant gas physics in both methods. Possible changes in the parameters of the predicted Y - M relation can be expected as models achieve greater realism.

4. CLUSTER DETECTION

To study cluster detection, three maps of the ACT strip are first created (combining the primary microwave background, infrared and radio point sources, and the full SZ effect) at the frequency channels of 145, 215, and 280 GHz. The ACT instrument is simulated by convolving the ACT strip maps at 145, 215, and 280 GHz with a Gaussian beam of FWHM equal to $1.7'$, $1.1'$, and $0.93'$, respectively. Gaussian random noise is then added to the maps of σ equal to 2, 3.3, and $4.7 \mu\text{K beam}^{-1}$ for the three frequencies, respectively. The above are preliminary detector noise estimates for extensive dedicated observations of the ACT strip. We produce a single map of the SZ clusters by applying a multi-frequency Wiener filter to the three ACT maps. This filter requires a model power spectrum of the first-order thermal SZ signal from the clusters (see eq. [6]). We first use a spectrum derived from the simulations themselves, and then one derived from the analytic prescription given by Komatsu & Seljak (2002) to test the sensitivity of the filter performance on the input cluster model. Clusters are then identified within the filtered map using a simple peak-finding algorithm. These clusters are matched to a catalog documenting the input map. From this matching process, we determine the completeness and purity of our detected cluster sample.

4.1. Multifrequency Wiener Filter

In the literature, a number of different filters have been employed to extract the SZ signal from microwave simulations (see introduction for references). Two commonly employed filters are matched or scale-adaptive filters and Wiener filters. Matched filters make an explicit assumption about cluster profiles, while Wiener filters assume knowledge of the SZ power spectrum. Both have qualitatively similar shapes: they suppress the primary microwave background at large scales and noise at small scales. Our motivation for choosing to use a Wiener filter stems from the fact that it recovers the minimum variance SZ map and is simple to implement. We compare our results with Melin et al. (2006), who employ a scale-adaptive filter, and find that a Wiener filter yields comparable results. We also use two different Wiener filters and find that the differences are minor.

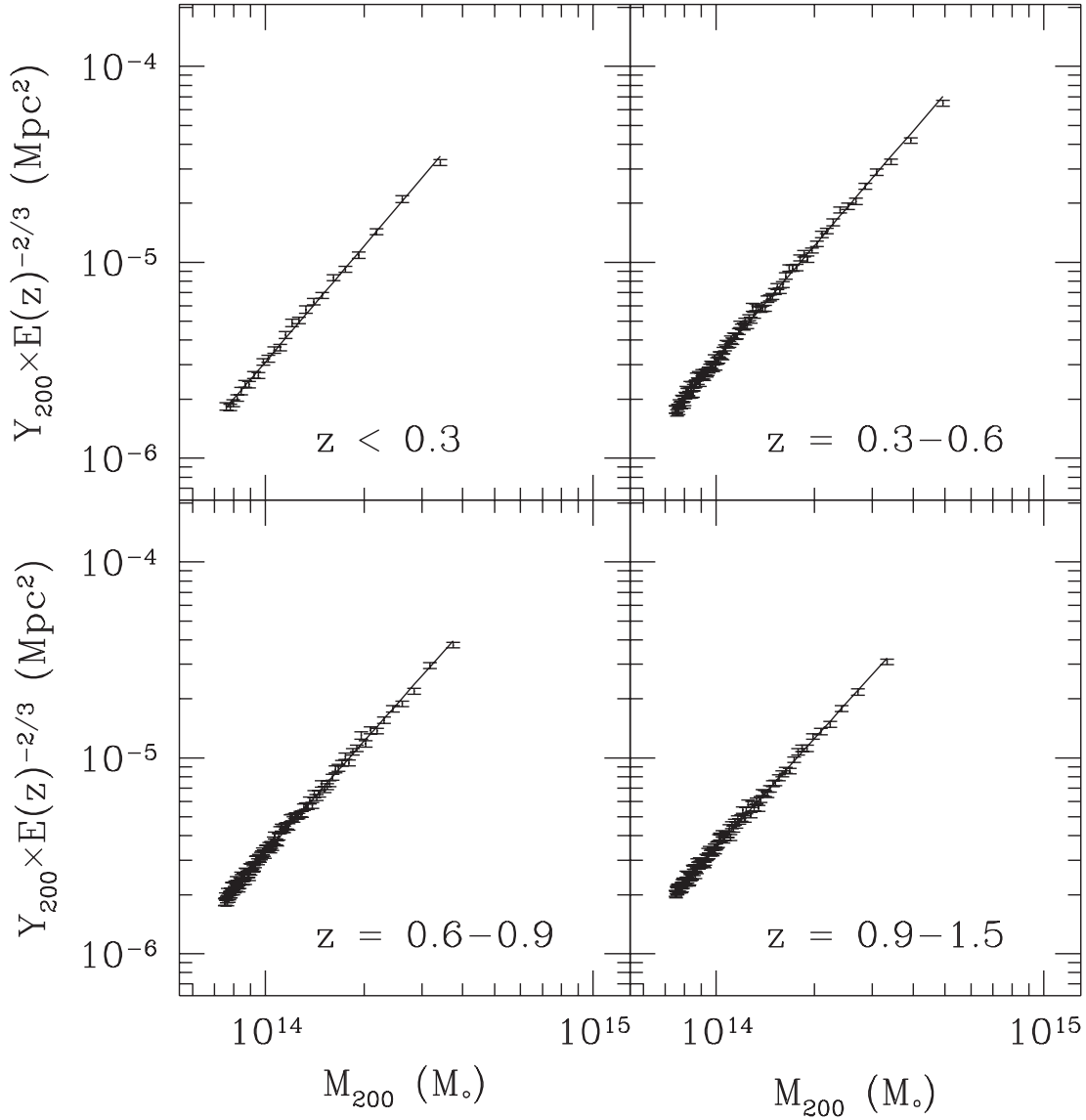


FIG. 6.— $Y_{200}E(z)^{-2/3}$ vs. M_{200} for four different redshift regions. As in Fig. 5, each point represents the mean of 250 clusters, and error bars represent the error on the mean. The parameters and reduced χ^2 for the best-fit lines are given in Table 2.

Below we describe the map filter in detail. We wish to recover one filtered map (of clusters) from several ACT maps (at three different frequencies). The latter are described by the data vector \mathbf{d} . We write $\mathbf{d} = \mathbf{R}\mathbf{s} + \mathbf{n}$, where \mathbf{R} is the instrument response to the Compton y signal map \mathbf{s} (see eq. [5]) and \mathbf{n} is the noise. In this notation, \mathbf{R} includes both the frequency dependence of the first-order thermal SZ signal (see eq. [6]) and the convolution with the beam. The noise \mathbf{n} includes detector noise, primary microwave background, point sources, and contributions to the SZ signal other than

from the first-order thermal SZ. We denote the covariance of the signal, noise, and data by $\mathbf{S} = \langle \mathbf{s}\mathbf{s}^\dagger \rangle$, $\mathbf{N} = \langle \mathbf{n}\mathbf{n}^\dagger \rangle$, and $\mathbf{D} = \langle \mathbf{d}\mathbf{d}^\dagger \rangle = \mathbf{R}\mathbf{S}\mathbf{R}^\dagger + \mathbf{N}$, assuming that signal and noise are largely uncorrelated.

The multifrequency Wiener filter is given by

$$\mathbf{W} = \mathbf{S}\mathbf{R}^\dagger(\mathbf{R}\mathbf{S}\mathbf{R}^\dagger + \mathbf{N})^{-1} = \mathbf{S}\mathbf{R}^\dagger\mathbf{D}^{-1}, \quad (13)$$

and it gives the least-squares signal map reconstruction via $\hat{\mathbf{s}} = \mathbf{W}\mathbf{d}$. Here we are assuming statistically homogeneous signal

TABLE 2
BEST-FIT PARAMETERS FOR THE BEST-FIT LINES DEPICTED IN FIGURES 5 AND 6, FITTED USING THE POWER LAW GIVEN IN EQUATION (12)

$M_{200} > 0.75 \times 10^{14} M_\odot$	α	σ_α	β	σ_β	Reduced χ^2	Clusters	Bins
$z > 0$	1.876	0.005	-5.4774	0.0009	1.004	90750	363
$z < 0.3$	1.96	0.02	-5.509	0.004	1.18	6250	25
$z = 0.3-0.6$	1.944	0.009	-5.502	0.002	1.38	24750	99
$z = 0.6-0.9$	1.88	0.01	-5.484	0.002	1.14	27250	109
$z = 0.9-1.5$	1.85	0.01	-5.457	0.002	1.02	27500	110
$z > 1.5$	1.82	0.05	-5.421	0.004	0.66	4250	17

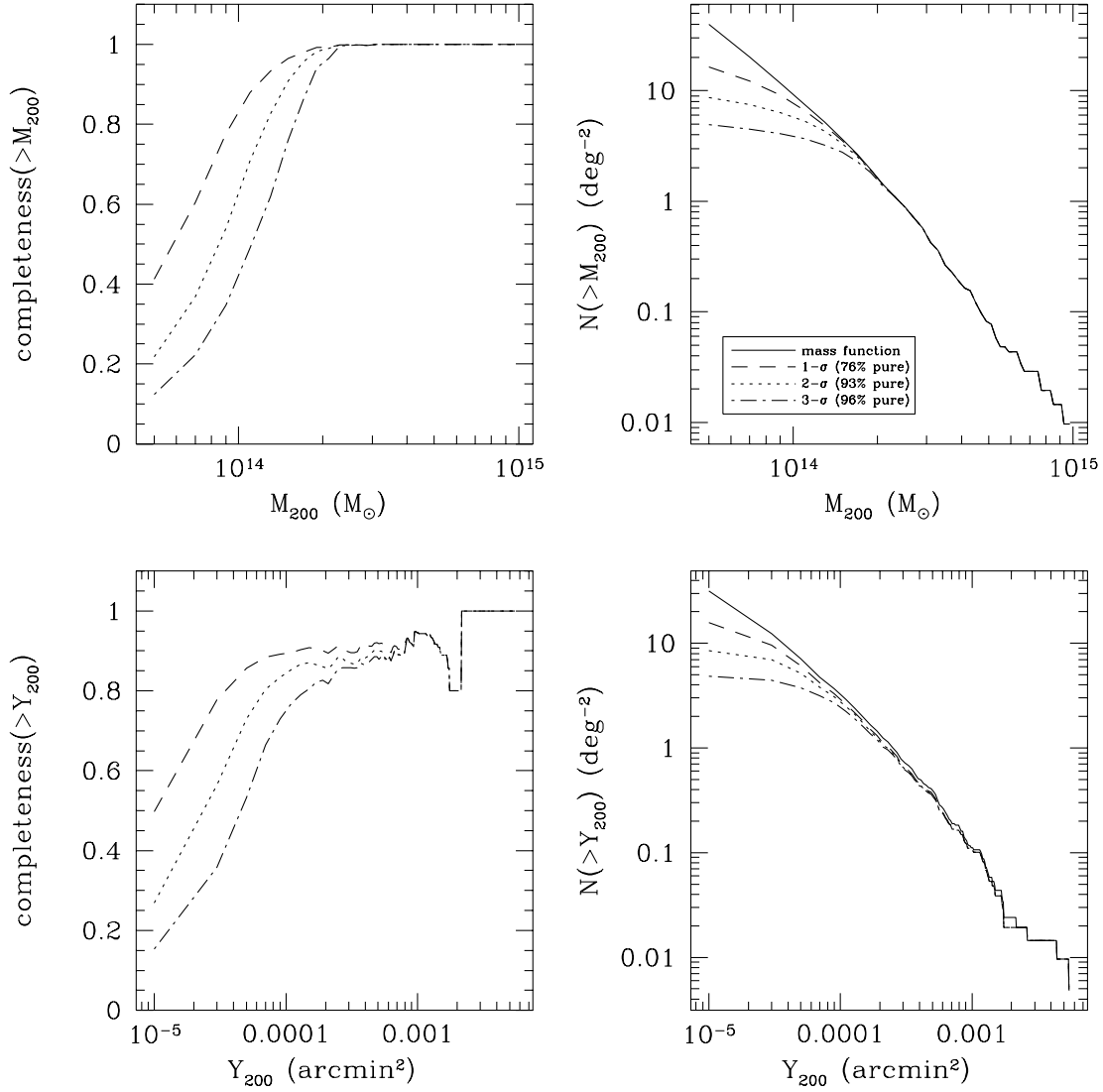


FIG. 7.—Completeness and purity of the detected cluster sample with ACT instrument specifications, in the case of no point sources. Different lines represent 1, 2, and 3 σ threshold cuts in the detection algorithm, where σ is the standard deviation of the filtered map. The solid line represents the simulation mass function. The purity of each cluster sample is given in the legend. See text for further details.

and noise, so all the covariances are (block) diagonal in the Fourier representation: they are the auto and (frequency) cross spectra. This makes the application of the Wiener filter straightforward: we Fourier transform the ACT maps, apply the filter, and inverse Fourier transform to obtain the SZ cluster map (for a useful reference on Wiener filtering see Tegmark & Efstathiou 1996).

4.2. Filtering Maps

To filter the maps, we divide the ACT strip (with SZ, primary microwave background, and point sources combined) into roughly $4^\circ \times 3.25^\circ$ patches. The above dimensions are chosen to give square patches in pixel space. To compute D , the power and cross power spectra for each patch are calculated and averaged over the whole strip. For the first model cluster power spectrum (S), we compute the spectrum from the simulations in a similar fashion. Later we also use the semianalytic spectrum of Komatsu & Seljak (2002).

To avoid aliasing of signal at the edges of each patch, we use an overlap-and-save method to filter overlapping pieces of the map. This permits us to discard all the vertical edges (edges of

constant right ascension) on the patch borders (Press et al. 1992). In this way, we remove any discontinuities in the filtered map at the boundaries of the patches. The horizontal edges are less of a concern since they can be discarded after the whole strip is filtered. This filtering procedure provides a filtered map of the entire ACT strip consisting of the recovered SZ signal.

4.3. Identifying Clusters

Clusters are identified by searching for all peaks in the filtered map above a given threshold value. The threshold cuts we apply are 1, 2, and 3 times the standard deviation of the filtered map. A peak is identified simply as a pixel larger than any pixel within a radius $r = 6p$ around it, where p is the pixel size ($p \approx 0.21'$ for these maps). We choose this radius both because $\approx 1.3'$ is a typical cluster size and in an effort to be consistent with Melin et al. (2006) for comparison purposes. Once a list of peaks is compiled, the peaks are matched to clusters in the input cluster catalog. We identify a match if the peak and catalog cluster are within a distance r of one another. Multiple peaks matching a single catalog cluster are allowed, as are multiple catalog clusters matching a single peak. Follow-up observations to determine cluster redshifts

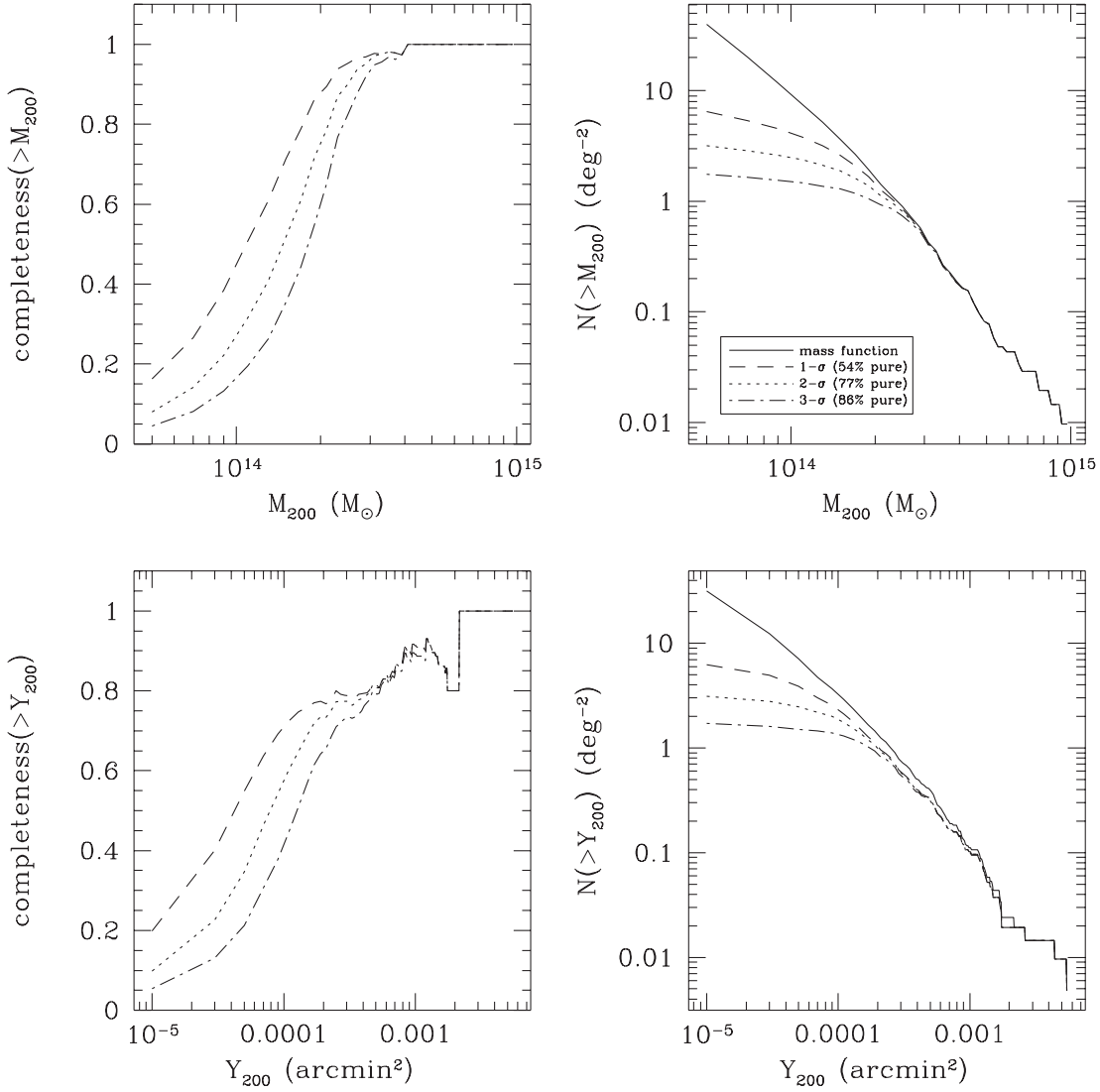


FIG. 8.—Completeness and purity of the detected cluster sample in the case of infrared point sources only.

should sort these cases out. Any peak that is not within r of any catalog cluster is flagged as a false detection.

It is possible that some peaks match catalog clusters just by chance alignment. However, since clusters down to only $5 \times 10^{13} M_{\odot}$ are included, all the clusters in the simulation are comparable to or above ACT instrument noise and thus are in principle detectable. So we accept that some small fraction of the simulation clusters may be detected by chance alignment with spurious peaks and do not try to distinguish these cases from real matches.

4.4. Results

First, we examine the case when the three-frequency ACT strip maps contain no radio or infrared point sources. The completeness and number of detected clusters per square degree are given in Figure 7 as a function of both M_{200} and Y_{200} (the latter measured as a solid angle in units of arcmin^2). The dashed, dotted, and dot-dashed lines represent the 1, 2, and 3 σ threshold cuts, respectively, and the solid line represents the simulation mass function. The purity of each cluster sample is given in the legend (purity: one minus the percentage of false-positive detections; completeness: number of detected clusters/number of input clusters). In the absence of point sources, using a 3 σ threshold cut, our sample of

detected clusters is 96% complete down to $2 \times 10^{14} M_{\odot}$ with only 4% contamination from false positives. The completeness as a function of Y_{200} and purity are comparable to that found by Melin et al. (2006) when they investigated a no-point-source case for the South Pole Telescope (SPT) using a matched filter and simulated clusters that perfectly matched their filter.

In the completeness versus Y_{200} plot, there is a sharp decrease in the completeness from 1 to 0.8 at $Y_{200} = 2 \times 10^3 \text{ arcmin}^2$. This effect is caused by a single cluster at $z \approx 0.04$ with $M_{200} \approx 8 \times 10^{13} M_{\odot}$. Since this cluster is so nearby, it extends over many pixels and thus has a large Y_{200} in units of arcmin^2 . However, its signal in each pixel is below that of the 1 σ threshold cut, so it is not detected. If the plot had been made with Y_{200} in units of physical area (Mpc^2), this feature would disappear. Therefore, this feature is an artifact reflecting the fact that arcmin^2 is not a unit intrinsic to a cluster. It also suggests that for detecting extended, low-redshift clusters, searching for a peak pixel is not the best method. Profile fitting may provide a better alternative in this case.

Next, infrared point sources are added to the three-frequency ACT maps following the prescription described in § 2.3. Infrared sources up to a flux limit of ≈ 0.4 Jy at 145 GHz are included since the number of sources with higher flux is effectively zero for the area of the ACT strip given the above prescription. Figure 8

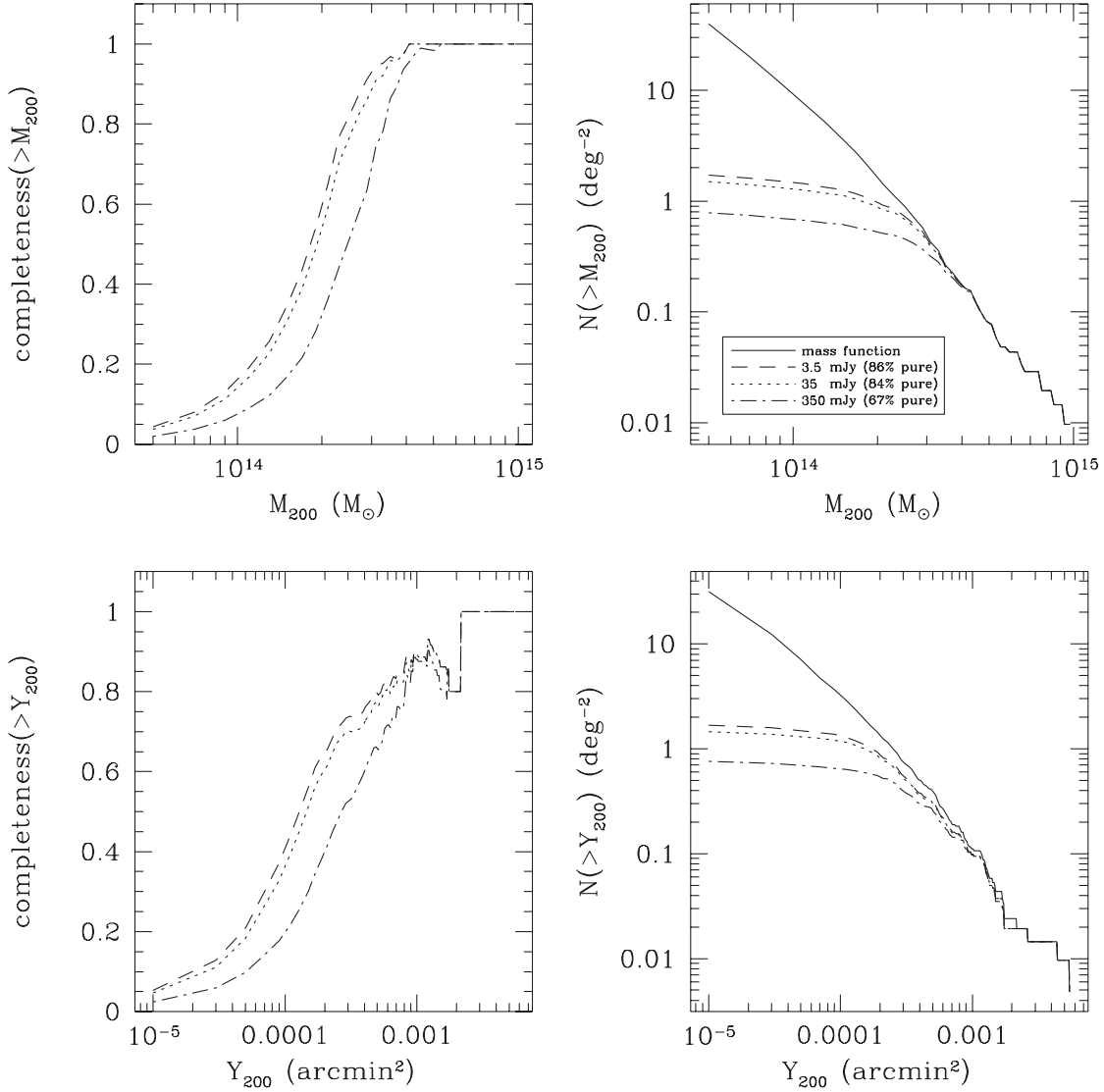


FIG. 9.—Completeness and purity when both infrared and radio sources are included. A 3σ cut is used for all the lines. The different lines represent different flux cuts at 145 GHz for the radio sources. If all the radio sources above 3.5 mJy at 145 GHz are removed from the three-frequency ACT maps, then we recover the results with only infrared point sources included. Removing all sources above 35 mJy at 145 GHz gives results that are only slightly degraded compared to the former case.

shows the cluster detection results after adding this population of point sources. For this case, using a 3σ threshold cut, the detected cluster sample is 95% complete down to $3 \times 10^{14} M_{\odot}$ with 14% contamination from false-positive detections. The percentage of false positives is comparable to that found by Melin et al. (2006) when they used N -body, as opposed to spherical, clusters for their no-point-source case. A direct comparison of completeness, including infrared point sources, with their work is difficult because we do not use isothermal, spherical clusters and we include clusters down to a lower mass limit, which crowds the field and increases confusion.

We further investigate the case where both infrared and radio point sources are added to the three-frequency ACT strip maps. The radio sources follow the prescription described in § 2.3. Figure 9 shows the cluster detection results including radio sources in the ACT maps below three different flux limits (3.5, 35, and 350 mJy at 145 GHz). All the lines correspond to cluster detection using a 3σ threshold cut. The dashed line shows that if all the radio sources above 3.5 mJy at 145 GHz are removed from the three-frequency ACT maps, the infrared-point-source-only case is recovered, depicted in Figure 8. If all the radio sources above

35 mJy at 145 GHz are removed from the three ACT maps, we obtain results that are of only slightly lower quality than the previous case. These results can be understood by noting that the inclusion of radio sources below 35 mJy and infrared sources increases the average power in the simulated ACT strip on scales of a few arcminutes by roughly an order of magnitude, as compared to not including point sources. The inclusion of all the radio sources above 35 mJy increases the power on these scales by several orders of magnitude more. This large increase in noise power is why these few very bright sources limit cluster detection with this technique. For an arcmin² beam at 145 GHz, 3.5 and 35 mJy correspond to ≈ 100 and $\approx 1000 \mu\text{K}$, respectively. Thus, achieving the removal of radio sources above the former flux limit may require interferometric observations of the ACT strip at a lower frequency (e.g., with the Australia Telescope Compact Array at ≈ 20 GHz). Achieving the latter flux limit of radio sources is most likely possible with ACT alone. (Sources of $\approx 1000 \mu\text{K}$ should be easy to identify, and we find ≈ 700 of them in our simulations of the ACT strip, which is not an unmanageable number to remove.) Assuming removal of radio sources above 35 mJy at 145 GHz, our detected cluster sample is 90% complete down to $3 \times 10^{14} M_{\odot}$ and 84% pure.

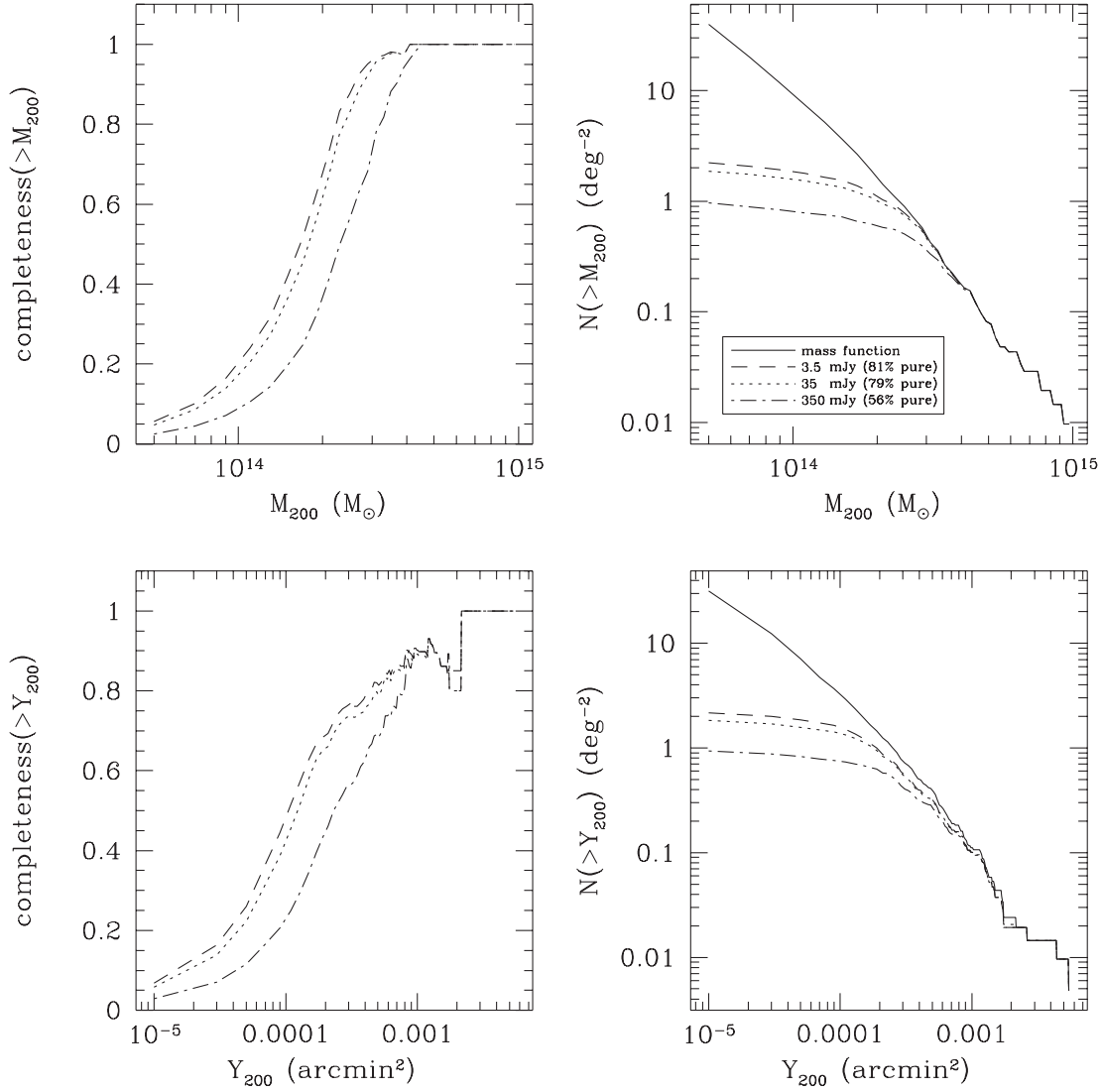


FIG. 10.—Completeness and purity of the detected cluster sample for the cases described in Fig. 9, but this time using a filter constructed with a cluster Compton y power spectrum derived analytically from Komatsu & Seljak (2002) instead of taken directly from the simulations. The completeness is slightly increased and the purity slightly decreased as compared to the previous figure, but overall the difference is small.

The filter used in obtaining the above results was created using the Compton y power spectrum from the simulations themselves. Since we shall not know beforehand the true cluster power spectrum, we remake the filter using a Compton y power spectrum derived analytically from the prescription in Komatsu & Seljak (2002). With this filter, we repeat the above exercise. Figure 10 displays the cluster detection results using this filter and adding both infrared and radio point sources. The different lines again correspond to the three different flux cuts of radio sources, and a 3σ threshold cut is used for them all. For the three flux cut cases, there is a slight increase in completeness of the cluster sample as compared to Figure 9. However, there is also a slight decrease in the purity of the cluster sample. If we compare the first-order thermal SZ power spectrum from the simulations and derived analytically (Fig. 4), we see that the filter made with the analytic power spectrum leaves more small-scale power in the filtered map. This increases the sample completeness but also decreases its purity, as more point sources are left in the map as well. Overall, however, the difference in using the analytic power spectrum in the filter, as compared to the power spectrum from the simulations, is small. This suggests that the performance of the

filter is not overly sensitive to how the cluster physics is modeled when constructing it.

5. FUTURE WORK

In this work, we did not correlate the radio and infrared point sources with the clusters. This was due to a lack of observational data regarding these correlations. If either population both is strongly correlated with clusters and exhibits a relatively flat spectrum between the infrared/radio regime and the microwave, then some further percentage of clusters may fail to be detected. Recent BIMA and OVRO observations targeting massive galaxy clusters at 28.5 GHz suggest an overabundance of mJy radio sources in these massive clusters as opposed to noncluster fields (Coble et al. 2007). However, they also find a steeper spectral index for these sources as compared to the brighter, rarer population of radio sources found by *WMAP* (Bennett et al. 2003b). If their spectral index steepens further above 30 GHz, these former sources may not be an issue. But if their slope flattens out, some of these sources may fill in the SZ decrement of some percentage of clusters at 145 GHz. Without a better understanding of these correlations and observations of these point sources in the range of

145–280 GHz, it is difficult to model both infrared and radio sources more realistically. Upcoming microwave surveys and follow-up or concurrent radio and infrared observations overlapping the survey areas will hopefully clarify these current unknowns. It is useful to keep in mind that, for constraining cosmology, obtaining a large number of detected clusters is less important than obtaining a solid understanding of the selection criteria. So if point sources affect cluster detection more significantly than anticipated, as long as this effect can be accurately characterized, it should not pose an overwhelming hurdle for cosmological investigations.

Some further avenues of investigation that we did not cover in this work include the following. The instrument noise can be more realistically modeled than we have done here, and atmospheric noise can be included. The lensing of the primary microwave background and point sources by clusters can be modeled to study its effect on cluster detection and SZ flux recovery. Moreover, the optimal recovery of cluster SZ flux, which is an issue distinct from cluster detection, should be investigated. This will aid in flux-mass identifications and SZ component separation. Some recent work addressing the latter issue can be found in Melin et al. (2006). We also by no means suggest that Wiener filtering is the ideal cluster detection tool, and further study in this direction is also warranted.

6. CONCLUSIONS

New microwave instruments have the potential to detect many galaxy clusters out to redshift $z = 1$ and beyond by their SZ signature. These galaxy clusters provide information about the growth of structure, which in turn constrains cosmology. However, the SZ signal is embedded within the signals from the primary microwave background, radio and infrared point sources that still have significant flux in the microwave regime, and galactic emission. Thus, in an effort to study the detection of clusters via their SZ effect, we simulated the microwave sky over both the proposed ACT observing region and a parallel strip centered at $\delta = -5^\circ$. To realistically model the small-scale cluster physics, which affects the SZ signal, we combined an N -body simulation with an analytic gas model (Ostriker et al. 2005; Bode et al. 2007). This allowed us to model cluster processes such as star formation and feedback over much larger volumes than can currently be achieved by hydrodynamic simulations. One product of these cluster simulations is that we are also able to study features in the SZ flux-mass scaling relation, such as its slope and normalization and their evolution with redshift. Knowledge of this relation is necessary to connect SZ flux to cluster mass, which is the quantity of interest for cosmology.

In investigating the relation between SZ flux and mass, roughly 10^5 clusters from our N -body plus gas simulations are fitted to the power-law relation given in equation (12). The best-fit power-law index is found to be $\alpha = 1.876 \pm 0.005$ and the reduced χ^2 to be 1.004. This slope is steeper than $5/3$, which is the expectation for the self-similar model. This steeper slope is consistent with the inclusion of feedback from both active galactic nuclei and supernovae in these simulations, which serves to lower the SZ flux more for lower mass clusters. This slope is understandably steeper than that for hydrodynamic simulations, which do not include feedback from active galactic nuclei and thus have a lower amount of overall feedback than in this simulation. We find some redshift dependence for both the power-law index and normalization of this relation. This is expected since clusters are not in fact self-similar and because star formation and cluster feedback are redshift dependent in our simulations. The steepening of the power-

law index at lower redshifts is consistent with more star formation and feedback occurring at later times. Considering only the higher mass clusters, $M_{200} > 2 \times 10^{14} M_\odot$, we find a flatter slope of $\alpha = 1.81 \pm 0.02$ with a reduced χ^2 of 1.14. We also see less obvious evolution of the slope and normalization with redshift. This is consistent with the higher mass clusters being less sensitive to feedback processes. It should be noted that the details of this Y - M relation can change as additional sources of nonthermal pressure support such as magnetic fields, cosmic rays, and turbulence are included in semianalytic gas models.

Our projections for cluster detection with the ACT instrument are also promising. Cluster detection was investigated under varying levels of point-source contamination utilizing a multifrequency Wiener filter and peak-finding algorithm. These results suggest that in the absence of point sources, considering only peaks above 3σ in the filtered map, ACT can obtain a cluster catalog that is 96% complete above $2 \times 10^{14} M_\odot$ and 96% pure (4% false detections). The inclusion of infrared sources results in a catalog that is 95% complete above $3 \times 10^{14} M_\odot$ and 86% pure. When all radio sources are included in addition, with no flux cutoff, we find that the noise from the brightest radio sources interferes significantly with cluster detection using this technique. However, if the brightest sources are removed from the ACT maps, there is a considerable improvement. Removing all radio sources above 35 mJy at 145 GHz from the three-frequency ACT maps results in a catalog that is 90% complete above $3 \times 10^{14} M_\odot$ and 84% pure. Removing all radio sources above 3.5 mJy at 145 GHz gives the same results as the inclusion of only infrared point sources. These results are encouraging, since 35 mJy sources should be easily identifiable and removable from ACT maps without need for further observations at alternate frequencies.

This study was repeated using a cluster model in our filter that differed from that in our simulations. Doing this produced only a small change in the cluster detection results. This suggests that the filter performance is not very sensitive to the details of the cluster model used to create it. As a result, efforts to characterize the selection function are made easier.

The potential of new microwave instruments to provide knowledge about cluster physics and cosmology is substantial, as our results further confirm. It is hoped that the simulations created to pursue the above studies will serve as a useful tool for future investigations toward making this potential a reality.

N. S. would like to thank Jack Hughes for many useful discussions and comments. The authors would also like to thank Jim Bartlett, Gil Holder, Arthur Kosowsky, Robert Lupton, J. P. Ostriker, Beth Reid, and David Spergel for useful discussions. This work was partially supported by the National Center for Supercomputing Applications under grant MCA04N002. In addition, computational facilities supported by NSF grants AST 02-16105 and AST 04-08698 were used, as well as high-performance computational facilities supported by Princeton University under the auspices of the Princeton Institute for Computational Science and Engineering (PICSciE) and the Office of Information Technology (OIT). N. S. acknowledges NSF PIRE grant OISE-0530095 and NASA LTSA NAG5-11714. H. T. was supported in part by NASA LTSA-03-000-0090, and K. H.'s portion of this work was partially performed at the Jet Propulsion Laboratory, California Institute of Technology, under a contract with the National Aeronautics and Space Administration.

REFERENCES

- Aghanim, N., de Luca, A., Bouchet, F. R., Gispert, R., & Puget, J. L. 1997, *A&A*, 325, 9
- Bahcall, N. A., & Fan, X. 1998, *ApJ*, 504, 1
- Barbosa, D., Bartlett, J. G., Blanchard, A., & Oukbir, J. 1996, *A&A*, 314, 13
- Bennett, C. L., et al. 2003a, *ApJS*, 148, 1
- . 2003b, *ApJS*, 148, 97
- Bertschinger, E. 2001, *ApJS*, 137, 1
- Birkinshaw, M. 1999, *Phys. Rep.*, 310, 97
- Bode, P., & Ostriker, J. P. 2003, *ApJS*, 145, 1
- Bode, P., Ostriker, J. P., Weller, J., & Shaw, L. 2007, *ApJ*, 663, 139
- Bode, P., Ostriker, J. P., & Xu, G. 2000, *ApJS*, 128, 561
- Borys, C., Chapman, S., Halpern, M., & Scott, D. 2003, *MNRAS*, 344, 385
- Calabretta, M. R., & Greisen, E. W. 2002, *A&A*, 395, 1077
- Carlstrom, J. E., Holder, G. P., & Reese, E. D. 2002, *ARA&A*, 40, 643
- Challinor, A., & Lewis, A. 2005, *Phys. Rev. D*, 71, 103010
- Coble, K., et al. 2007, *AJ*, 134, 897
- da Silva, A. C., Kay, S. T., Liddle, A. R., & Thomas, P. A. 2004, *MNRAS*, 348, 1401
- Dolag, K., Bartelmann, M., & Lesch, H. 1999, *A&A*, 348, 351
- Eke, V. R., Cole, S., & Frenk, C. S. 1996, *MNRAS*, 282, 263
- Finkbeiner, D. P., Davis, M., & Schlegel, D. J. 1999, *ApJ*, 524, 867
- Górski, K. M., Hivon, E., Banday, A. J., Wandelt, B. D., Hansen, F. K., Reinecke, M., & Bartelmann, M. 2005, *ApJ*, 622, 759
- Güsten, R., et al. 2006, *Proc. SPIE*, 6267, 37
- Haiman, Z., Mohr, J. J., & Holder, G. P. 2001, *ApJ*, 553, 545
- Herranz, D., Sanz, J. L., Barreiro, R. B., & Martínez-González, E. 2002a, *ApJ*, 580, 610
- Herranz, D., Sanz, J. L., Hobson, M. P., Barreiro, R. B., Diego, J. M., Martínez-González, E., & Lasenby, A. N. 2002b, *MNRAS*, 336, 1057
- Hinshaw, G., et al. 2007, *ApJS*, 170, 288
- Horner, D. 2001, Ph.D. thesis, Univ. Maryland
- Jenkins, A., Frenk, C. S., White, S. D. M., Colberg, J. M., Cole, S., Evrard, A. E., Couchman, H. M. P., & Yoshida, N. 2001, *MNRAS*, 321, 372
- Juin, J. B., Yvon, D., Réfrégier, A., & Yèche, C. 2007, *A&A*, 465, 57
- Kneissl, R., Jones, M. E., Saunders, R., Eke, V. R., Lasenby, A. N., Grainge, K., & Cotter, G. 2001, *MNRAS*, 328, 783
- Knox, L., Holder, G. P., & Church, S. E. 2004, *ApJ*, 612, 96
- Komatsu, E., & Seljak, U. 2002, *MNRAS*, 336, 1256
- Kosowsky, A. 2003, *NewA Rev.*, 47, 939
- Li, C.-T., et al. 2006, *Proc. SPIE*, 6275, 49
- Lima, M., & Hu, W. 2005, *Phys. Rev. D*, 72, 043006
- Majumdar, S., & Mohr, J. J. 2003, *ApJ*, 585, 603
- . 2004, *ApJ*, 613, 41
- McCarthy, I. G., Balogh, M. L., Babul, A., Poole, G. B., & Horner, D. J. 2004, *ApJ*, 613, 811
- Melin, J.-B., Bartlett, J. G., & Delabrouille, J. 2005, *A&A*, 429, 417
- . 2006, *A&A*, 459, 341
- Motl, P. M., Hallman, E. J., Burns, J. O., & Norman, M. L. 2005, *ApJ*, 623, L63
- Nagai, D. 2006, *ApJ*, 650, 538
- Nagamine, K., Ostriker, J. P., Fukugita, M., & Cen, R. 2006, *ApJ*, 653, 881
- Nozawa, S., Itoh, N., & Kohyama, Y. 1998, *ApJ*, 508, 17
- Ostriker, J. P., Bode, P., & Babul, A. 2005, *ApJ*, 634, 964
- Oukbir, J., & Blanchard, A. 1992, *A&A*, 262, L21
- Pfrommer, C., Ensslin, T. A., Springel, V., Jubelgas, M., & Dolag, K. 2007, *MNRAS*, in press
- Pierpaoli, E., Anthoine, S., Huffenberger, K., & Daubechies, I. 2005, *MNRAS*, 359, 261
- Press, W. H., Teukolsky, S. A., Vetterling, W. T., & Flannery, B. P. 1992, *Numerical Recipes in C* (2nd ed.; Cambridge: Cambridge Univ. Press)
- Rasia, E., Tormen, G., & Moscardini, L. 2004, *MNRAS*, 351, 237
- Reiprich, T. H., & Böhringer, H. 2002, *ApJ*, 567, 716
- Rosati, P., Borgani, S., & Norman, C. 2002, *ARA&A*, 40, 539
- Ruhl, J., et al. 2004, *Proc. SPIE*, 5498, 11
- Runyan, M. C., et al. 2003, *ApJS*, 149, 265
- Schaefer, B. M., & Bartelmann, M. 2007, *MNRAS*, 377, 253
- Schlegel, D. J., Finkbeiner, D. P., & Davis, M. 1998, *ApJ*, 500, 525
- Schulz, A. E., & White, M. 2003, *ApJ*, 586, 723
- Spergel, D. N., et al. 2007, *ApJS*, 170, 377
- Stolyarov, V., Hobson, M. P., Ashdown, M. A. J., & Lasenby, A. N. 2002, *MNRAS*, 336, 97
- Sunyaev, R. A., & Zel'dovich, Y. B. 1970, *Comments Astrophys. Space Phys.*, 2, 66
- . 1972, *Comments Astrophys. Space Phys.*, 4, 173
- Tauber, J. A. 2004, *Adv. Space Res.*, 34, 491
- Tegmark, M., & Efstathiou, G. 1996, *MNRAS*, 281, 1297
- Vale, C., & White, M. 2006, *NewA*, 11, 207
- Viana, P. T. P., & Liddle, A. R. 1996, *MNRAS*, 281, 323
- Wang, L., & Steinhardt, P. J. 1998, *ApJ*, 508, 483
- Wang, S., Khoury, J., Haiman, Z., & May, M. 2004, *Phys. Rev. D*, 70, 123008
- Weller, J., & Battye, R. A. 2003, *NewA Rev.*, 47, 775
- Weller, J., Battye, R. A., & Kneissl, R. 2002, *Phys. Rev. Lett.*, 88, 231301
- White, M. 2003, *ApJ*, 597, 650
- White, M., Hernquist, L., & Springel, V. 2002, *ApJ*, 579, 16
- Younger, J. D., Haiman, Z., Bryan, G. L., & Wang, S. 2006, *ApJ*, 653, 27